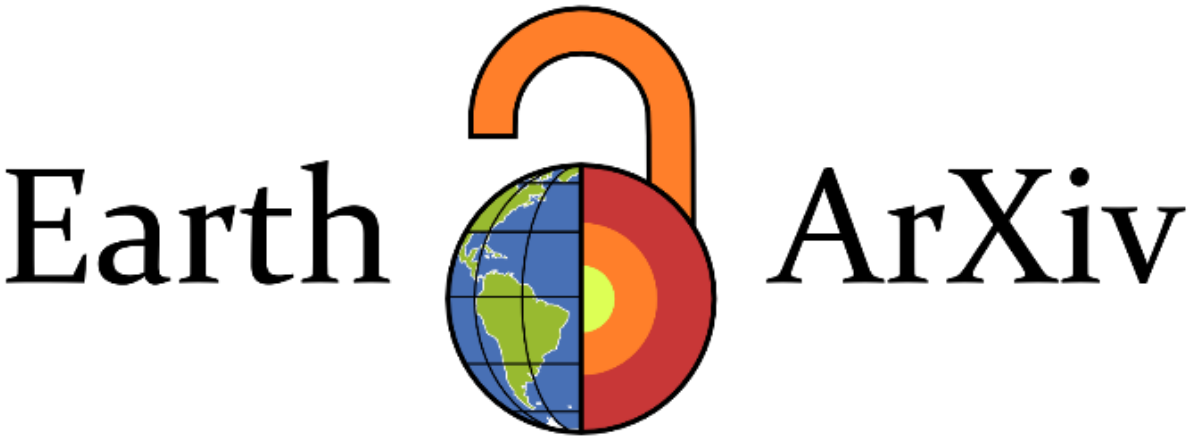

Formation and alteration of magnesite nodules from Kunwarara, Queensland, Australia, as an analogue to Mg-carbonate formation on Mars

E.L. Cardarelli[1,2]*, T.M. Present[2], P.M. Vasconcelos[4], L.C. Kah[1], C. Swindle[3,6], S. Bhattacharjee[3], and K. Farley[3]

[1]Department of Earth, Planetary, and Space Sciences, University of California, Los Angeles, Los Angeles, CA 90095, USA.

[2]Jet Propulsion Laboratory, California Institute of Technology, Pasadena, CA 91101, USA.

[3]Division of Geologic and Planetary Sciences, California Institute of Technology, Pasadena, CA 91125, USA.

[4]The University of Queensland, Queensland, Australia.

[5]Department of Earth, Environmental and Planetary Sciences, University of Tennessee, Knoxville, TN 37996, USA.

[6]Department of Materials Science and Engineering, University of California, Los Angeles, Los Angeles, CA 90095, USA.

Corresponding author: Emily Cardarelli (ecardare@epss.ucla.edu)

Key Points:

- An Australian vertisol overlying a magnecrete horizon hosts multi-generational Mg-carbonate nodules.
- Mg-rich groundwaters in Central Queensland precipitate carbonate minerals that display textures analogous to those of Mg-carbonates analyzed in Jezero crater, Mars.
- Magnecrete genesis and alteration reflect an interplay of biotic, hydrologic, and sedimentary processes relevant to astrobiology on Mars.

Abstract

Magnesite ($MgCO_3$) is a magnesium carbonate mineral that records the aqueous environmental conditions of its formation. On Earth, magnesite forms in metamorphic, diagenetic or pedogenic environments, and distinguishing between these environments is critical for understanding the nature of fluid chemistry during magnesite precipitation. Magnesite has been identified across the Nili Fossae region on Mars and in Jezero crater by orbital spectroscopic observations and in-situ instrument observations acquired with the *Perseverance* rover. Core samples with magnesite may provide constraints on the chemical conditions of the ancient aqueous environments of Jezero crater, and may also be an important phase to target for the preservation of potential biosignatures. This work explores pedogenic magnesite phases found in Vertisols of the Kunwarara Mine, Australia, as a potential analog environment for magnesite identified within Jezero crater, Mars. We document the principal microtextures and investigate the processes involved in the formation and diagenesis of magnesite nodules and magnecretes. Kunwarara magnesite nodules show complex textural relationships at the outcrop scale, and these relationships extend to the nanoscale in samples that were collected along a depth profile. By characterizing textural and chemical variations in magnesite at different scales, this work reveals a continuum between diagenetic and pedogenic magnesites. It illustrates that diagenetic reactions produce magnesite from ascending Mg^{2+}-rich groundwater interacting with detrital phases; groundwater interaction with descending meteoric solutions result in the conversion of magnesite into authigenic dolomite. Overall, this work shows how the superposition of textures and elemental compositions permits reconstruction of pedogenic processes leading to magnesite authigenesis.

Plain Language Summary

Magnesite is an important yet understudied carbon-storing mineral on Earth. It has been detected on Mars in the Nili Fossae Region and within Jezero crater using orbital spectroscopy and instruments aboard the *Perseverance* rover. By studying magnesite occurrences on Earth, we can obtain valuable information about the chemical changes that might have occurred in the past environments of Jezero crater. Critically, magnesite is a phase that forms under habitable conditions from water and carbon, potentially preserving evidence of ancient extraterrestrial life. To this end, magnesite at Jezero crater has been sampled for return to Earth. This study investigates magnesites from the Kunwarara deposit in Australia, which display similar textural features to those found in Jezero crater. Small-scale features of magnesite are examined here, with a particular focus on how magnesite precipitates and changes over time. Importantly, the work shows that primary magnesite can transform into other mineral phases, such as dolomite, through interactions with surficial waters. By studying the textures and chemical composition of magnesite samples on Earth, scientists can better understand the processes that led to the formation of magnesite in Jezero crater, Mars.

1 Introduction

The formation of magnesium (Mg) carbonate minerals is one mechanism which links both the carbon and water cycles. Mg-carbonate phases include amorphous magnesium carbonate, dolomite ($CaMg(CO_3)_2$, magnesite ($MgCO_3$), and various hydrous carbonates such as

nesquehonite ($MgCO_3 \cdot 3H_2O$) and hydromagnesite ($Mg_5(CO_3)_4(OH)_2 \cdot 4H_2O$). On Earth, Mg-carbonate phases form in a variety of settings, including as an alteration phase within ultramafic complexes, as a primary pedogenic phase within soils, as a diagenetic phase within soils and playas, and as a primary chemical precipitate within Mg-rich lakes and hydrothermal solutions (Pohl, 1989; Scheller et al., 2021). They have been studied in ultramafic (Falk & Kelemen, 2015; García Del Real & Vishal, 2016; Swindle, Vasconcelos, Dimarco, et al., 2025), lacustrine (Braithwaite and Zedef, 1996; Raudsepp et al., 2024; Valdespino-Castillo et al., 2022), marine (Lumsden, 1988), and playa environments (Mavromatis et al., 2021; Power et al., 2019). Outside Earth, Mg-carbonate phases have also been detected within martian meteorites such as ALH84001 (Mittlefehldt, 1994; Steele et al., 2022) and observed on Mars by orbital spectroscopy (Ehlmann et al., 2008; Horgan et al., 2020) as well as by in-situ rover observations (Kalucha et al., 2024; Scheller et al., 2022; Srivastava in prep). The occurrences of Mg-carbonate phases on Mars are thought to have been formed primarily in subsurface diagenetic settings (Scheller et al., 2021), which have fewer terrestrial analogs. However, the key controls on magnesite formation, such as the pressure/temperature conditions, relative time of formation, and effects of burial diagenesis – all remain poorly constrained.

On Earth, carbonate minerals which form at the interface between the hydrosphere, biosphere, atmosphere, and solid Earth are typically calcium (Ca) rich (A.M. Alonso-Zarza & Wright, 2010; Bachman & Machette, 1977; Goudie, 1983) and accumulate through time in pedogenic environments as calcretes. Magnesite, although less common, often occurs as weathering products of ultramafic rocks through low-temperature processes in semi-arid to arid environments (Oskierski et al., 2019; Power et al., 2019) and have a higher predicted solubility than Ca carbonates (Catling, 1999). The relative paucity of Mg-carbonates compared to Ca carbonates reflects Ca enrichment in Earth's continental crust; in contrast, weathering of Ca-poor ultramafic protoliths, such as those that are more common on Mars, preferentially generates Mg-carbonates.

Terrestrial calcrete forms in two primary ways. Pedogenic calcrete form where Ca-rich waters infiltrate into soil horizons, precipitating carbonate minerals along the infiltration pathway (A.M. Alonso-Zarza & Wright, 2010). Groundwater calcrete, in turn, form when Ca-rich waters ascend from the groundwater table through evapotranspiration and capillary action, forming extensive carbonate cement horizons with nodular facies towards the top of the (Alonso-Zarza, 2003). Previous studies have documented pedogenic and diagenetic dolomites and magnesites (Pohl, 1989).

This work examines Mg-carbonate-bearing rocks and soils of the Kunwarara area of central Queensland, Australia. Here, late Precambrian serpentinite and diverse Phanerozoic crustal igneous, metamorphic, and sedimentary rocks surround a hydrologic catchment that has been filled by late Cenozoic fluvial sediments. These sediments have developed into Mg-carbonate bearing Vertisol profiles resulting from pedogenic alteration over prolonged periods of time (Lin, 2011; Milburn & Wilcock, 1998; Swindle, Vasconcelos, Dalleska, et al., 2025). Mg-carbonate within these materials is hypothesized to be derived via a combination of pedogenic (i.e., authigenic reactions occurring in the soil) precipitation and secondary alteration processes. Neoformed magnesite occurs as both discrete nodules within arkosic sand and expandable clay, and as extensive stratiform bodies, similar to those observed at the nearby

Yaamba Mine (Swindle et al., 2025). These occurrences provide an ideal opportunity to trace the physicochemical processes leading to the precipitation of magnesium carbonates from low-temperature Mg-bearing solutions coupled to subsequent groundwater alteration and evolution of the substrate. By identifying microscale textural and chemical variation within the magnesites of Kunwarara, this work documents the occurrence of multiple magnesite types that are useful analogues for understanding genesis of Mg-carbonates detected at Jezero crater, Mars.

Here, we use a suite of integrated analytical techniques, including scanning electron microscopy (SEM), X-ray fluorescence mapping (XRF) and X-ray diffraction (XRD) analyses, to define the mineralogical and chemical variation of the magnesite and associated sediment collected across the Kunwarara weathering horizons. By leveraging measurements from the outcrop (meter-scale) to nanometer-scale, this work identifies and characterizes textural and chemical variation in the magnesite and other pedogenic minerals to reconstruct the genesis and evolution of these complex Mg-carbonate bearing assemblages.

2 Materials and Methods

2.1 Geologic setting

Magnesite occurs in both ultramafic and sedimentary rocks throughout the New England Fold Belt in eastern Australia (Oskierski et al., 2013, 2019; Swindle et al., 2025; Swindle et al., 2025). The Kunwarara quarries of central Queensland, Australia host some of the largest cryptocrystalline sedimentary magnesite deposits in the world (Milburn & Wilcock, 1998). This area is surrounded by the Princhester Serpentinite, a deeply weathered ultramafic bedrock that is assumed to be the primary source of regional aqueous weathering products (McNeil & Raymond, 2013; Swindle et al., 2025). The late Precambrian Princhester Serpentinite complex was emplaced within the New England Fold Belt during the early-mid Paleozoic. The serpentinite was later intruded, metamorphosed, and deformed by the Permo-Triassic aged Hunter-Bowen Orogeny (Bruce & Niu, 2000; Evans & Roberts, 1979; Murray, 2007). Cenozoic weathering and erosion of the Queensland passive margin then led to deep, lateritic weathering of bedrock (Batianoff & Singh, 2001; Foster et al., 2002; Zeissink, 1969) followed by Neogene to recent sediment deposition and pedogenesis of fluvial-alluvial sedimentary strata under less intense arid to semi-arid weathering conditions (e.g., Vertisol-forming climates) (Batianoff & Singh, 2001; Forster & Baker, 1997). The field site (red diamond, Figure 1) hosts deep overlying clays on alluvial plains that experience seasonally wet conditions (dark grey unit, Figure 1B). These sedimentary units are represented by unlithified arkose, subarkose, and lithic arenite sands and mud capped by a smectitic Vertisol of variable thickness and composition. Below the smectitic soil, within the bedded sand, magnesite occurs as centimeter- to decimeter-scale nodules and meter-scale stratiform bodies near the modern watertable (Figure 2, Figure 3).

2.2 Sample collection and analysis

Samples were collected from a 12-m Vertisol exposed at the edge of a magnesite mine pit within the Kunwarara Qmag magnesite mine (centered at 22° 55’ S, 150° 13’E, Kunwarara, Queensland, Australia, Figure 1) in August 2019. At the field site (red diamond, Figure 1), dark clays were found above friable, nodular magnesite in the upper subsection (Figure 2A) and

cemented magnesite in the lower subsection (Figure 2B). At the outcrop scale, six pedogenic horizons (19-AUS-20: 0-6.8 m depth belowground surface (bgs), 19-AUS-19: 6.8-8.3 m bgs, 19-AUS-24: 8.3-9.3 m bgs; Table S1) were identified. In each of these intervals, the host sediment as well as magnesite was sampled where present (Figure 2, Table S1). Magnesite was not found in the surface horizon (19-AUS-20) and host sediment was not retrieved from the deepest exposed horizon (19-AUS-21). Magnesite nodule samples were photographed at the Jet Propulsion Laboratory (JPL) and thin-sectioned (24 x 46 mm dimensions) by Wagner Petrographic for microscopy.

X-ray diffraction of the samples provided the initial assessment of the mineralogy of the magnesite and host sediment compositions. Subsamples of the magnesite and the host sediment were air-dried and homogenized with a mortar and pestle prior to XRD. The magnesite samples from the section transect were characterized with the Rigaku SmartLab XRD instrument in the California Institute of Technology Beckman Institute X-Ray Powder Crystallography Facility. In addition, sediment samples from the following horizons (19-AUS-20, 19-AUS-19, 19-AUS-24, 19-AUS-23, 19-AUS-22) were characterized by K/T Geosciences, Gunnison, CO on a Siemens D500 automated powder diffractometer equipped with a copper X-ray source (40kV, 30mA) and a scintillation X-ray detector. For bulk sediment XRD analysis, homogenized powder for each sample was dried, disaggregated, and then loaded into a metal sample holder to produce random bulk mounts. The bulk powder samples were analyzed over an angular range of 5° to 6° 2θ at a scan rate of 1° per minute, producing the air-dried treatment results. The clay mounts were then exposed to ethylene glycol vapor for a minimum of 12 hours and then analyzed by XRD again to determine clay mineral swelling in the glycolated, oriented clay-fraction. The air-dried and glycolated XRD patterns for each sample were compared for clay mineral identifications, and used to produce semi-quantitative determinations of mineral proportions from the bulk analyses with Jade Software (Materials Data, Inc., Livermore, CA) and the Whole Pattern Fitting option.

Polished thin sections and sample chips were used to characterize the fabric of magnesite samples as well as the spatial distribution of mineralogical components. Petrographic observations in plane and polarized light were conducted on polished thin sections at the California Institute of Technology on a Leica DM 2500 P microscope and at the University of Tennessee on an Olympus BX-60 microscope. Scanning electron microscopy (SEM) and energy dispersive x-ray spectroscopy (EDS) measurements were completed in the JPL Astrobiogeochemistry Laboratory on polished thin sectioned magnesite samples and sample chips with a Hitachi SU 3500 VP-SEM under high vacuum mode with a dispersive spectroscopy system by Oxford Instruments X-MaxN for automated elemental mapping and point analysis. SEM of the sediment material from the respective horizons sampled was completed in the Geological and Planetary Sciences (GPS) Analytical Facility at the California Institute of Technology with a Field Emission Scanning Electron Microscope (FE SEM) (Zeiss 1550 VP, operating in secondary electron (SE) and backscattered electron (BSE) modes at 15kV and 9 mm working distance on material pressed to carbon tape and coated with graphite. Elemental distributions were also mapped on the off-cut billets of the magnesite thin-sections in the Caltech GPS Analytical Facility using micro-X-ray fluorescence (μXRF) with a Bruker M4 Tornado

operating at 2 mbar vacuum with a 20 µm pixel size, 1 ms dwell time, and a rhodium X-ray tube powered to 50 kV and 600 µA.

3. Results

Composition and occurrence of the vertisol hosted sediments and magnesites

3.1 Composition and textural relationships of Kunwarara sediments

At the outcrop scale, the Vertisol examined is made up of an upper subsection (19-AUS-20, 19-AUS-19, 19-AUS-24) (Figure 2A, Figure 2B) and an offset lower subsection (19-AUS-23, 19-AUS-22, 19-AUS-21) (Figure 2E)separated by a mine pit terrace near the 19-AUS-24 horizon (Figure 2C, Figure 2D). The top subsection (~ 6.8 m) of the profile is dark and contains cracks with manganese oxide nodules (19-AUS-20). With depth, the profile grades from dark brown (19-AUS-20) to a greenish-gray and brown clay horizon with millimeter-scale light colored carbonate nodules (19-AUS-19). In the lower subsection, the sediments are light gray sandy clays with manganese oxides precipitated along blocky cracks (19-AUS-24 and 19-AUS-23), and weakly indurated clayey, silty, very fine sand hosting the most developed magnesite nodules (19-AUS-22 and 19-AUS-21) (Figure 2, Table S1, Table S2).

In all samples, clay minerals were the dominant constituent of the sediments. XRD data indicated that the swelling clays were predominantly dioctahedral Al-smectites (i.e., montmorillonites) that were poorly ordered and contained little to no illite interlayers (Table S1, Figure S1, Figure S2). Small amounts of talc, illite, and kaolinite were also detected through the profile (Table S2). The upper subsection is also dominated by smectite, though quartz is a major mineralogic component too (Figure S1, Figure S2). The quartz was likely authigenic as sand-sized grains in this horizon were rare (Figure 2, Table S1). Minor dolomite and magnesite were detected by XRD in the sediment matrix of the upper samples, despite the low abundance of larger magnesite nodules (Figure S2, Table S2). Palygorskite was also detected in the sediment matrix (Figure S2, Table S2) at the bottom of the upper subsection (19-AUS-24) (Figure 2).

In SEM images, the dolomite was observed to form micron-scale discs (Figures 6B, 7A, 7C, 7F) and the magnesite formed micron-scale rhombohedra (Figure 6, Figure 7A and 7F). Other authigenic minerals, not detected in XRD data, were observed with SEM, including Mn-oxides coating clays and authigenic cerianite ($(Ce, Th)O_2$) (Figure S1). In the gradational horizon near the base of the upper subsection (19-AUS-19: 6.8 to 8.3 m bgs), wavy subhedral expandable clays overgrew an etched quartz grain. Also observed were potential fungal hyphae attached to ilmenite (Figure S3).

XRD, XRF, and SEM/EDS of the sediments showed that the sand in the lower subsection is quartz-dominated to arkosic in composition. In the sandy lower subsection, the greatest proportion of quartz is present at the base and declines upwards. Quartz is present primarily as detrital silt and sand-sized grains, which are pitted and exhibit evidence of dissolution suggesting that their origin is partly detrital and alteration has occurred (Figure 6H). The lower sediment samples also contain variable amounts of additional immature detrital minerals

(serpentine, plagioclase, potassium feldspar, and lizardite) that are not found in the upper portions of the profile. Clay minerals rim detrital grains, including quartz, feldspars, and heavy minerals (ilmenite and chromite which were observed with SEM but not abundant enough for XRD detection) (Figure S1). In addition to smectite, small amounts of palygorskite was detected in the lower subsection, and it declines in abundance from top to bottom. With SEM/EDS, both of these phases had microtextures of neoformed, authigenic clays including platey, wavy, or flakey smectite (Bohor & Hughes, 1971) and spikey, fibrous palygorskite (Kaplan et al., 2014).

Swelling clays (smectite and mixed layer illite/smectite) dominate the composition of the upper profile subsection examined, followed by quartz (Figure S1, Table S2, Figure S2). The upper subsection sediment also contains variable proportions of lizardite, plagioclase, potassium feldspar, dolomite, magnesite, hematite and other clays (illite/mica, kaolinite, palygorskite, talc). Mn-oxides are also present as clay coatings. Dolomite, magnesite, and talc are only found in the sediment matrix of the upper subsection samples (Figure S3).

Overall, two major clay textures exist: (1) platey and wavy/flakey that we identify as smectite (Bohor & Hughes, 1971); and (2) spikey/fibrous, which we identify as palygorskite (Kaplan et al., 2014). Near the top of the profile (19-AUS-19), the presence of wavy subhedral expandable clays (kaolinite) over etched quartz grains and Fe-Al clays bordered by other clays as well as Mg-carbonates (rhombohedral magnesite and dolomite, Figure S3). Magnesite from multiple depths also contains petrographic evidence for detrital quartz dissolution and associated K-feldspar (Figure 2). These observations suggest that the highest degree of weathering is near the top of the soil profile (Figure 7). Clay minerals rim detrital grains, including quartz and feldspar. Rare earth elemental compositions of the sediments match magnesite found in the 19-AUS-19 – therefore an authigenic origin and neoformation is suggested for the overlying clays (Figure 7, Table S4).

3.2 Composition and occurrence of the Kunwarara magnesite nodules

Magnesium carbonate occurs as a rare, micron-scale constituent of the uppermost black soil, but they form nodules that increase in size from millimeter- to decimeter-scale with depth below 6.8 m bgs (Figure 2). Magnesium carbonate exhibits variable morphologies, including cauliflower-like nodules, columnar concretions, and subhorizontal indurated horizons. Bulk powder XRD analyses determined that the samples were dolomitic magnesite at the base of the upper subsection (19-AUS-19 and 19-AUS-24). Importantly, the Mg-carbonates occurrences were pure magnesite in the lower subsection (19-AUS-23, 19-AUS-22, and 19-AUS-21) (Figure 4, Figure S2).

In the uppermost magnesite-containing horizons (19-AUS-19 and 19-AUS-24) of the upper subsection, Mg-carbonate= is present as porous, friable, heterogeneous aggregates of magnesite and dolomite mixed with clay, oxide minerals, and siliciclastic sand grains. The aggregates are bright white and contain 100 µm to centimeter-scale glaebules that are light gray. Petrographic investigation reveals multiple types of glaebules (i.e. multidimensional entities in the soil matrix with a pedogenic origin) (Brewer & Sleeman, 1964) or micronodules hosted within the magnesite matrix. These multigenerational fabrics are comprised of ~2-4 µm

subhedral rhombohedral magnesite crystals and discoidal or anhedral dolomite microcrystals (Figure 5); both phases exhibit nanoscale intercrystalline porosity. Magnesite micronodules have discrete edges that are defined by a rim of equant magnesite crystals that are generally smaller in size. By contrast, dolomite micronodules are composed of densely packed, limpid (clear) lensoid crystals. Dolomite lenses also occur within microcrystalline magnesite as well as scattered through the magnesite matrix. They are interspersed with microcrystalline magnesite, detrital phases, Fe-oxyhydroxides, and authigenic clays (Figure 4, B-D). Detrital quartz and plagioclase included in the aggregates have distinctive embayed margins and pitting associated with their dissolution, and other detrital components that are replaced by chalcedony or Fe-oxyhydroxides. Amorphous silica and chalcedony also line pores in magnesite aggregates. The uppermost magnesite (19-AUS-19) is porous, with void spaces and loosely packed phases visible with SEM/EDS. At this depth, dolomite closely co-occurs with microcrystalline magnesite nodules that are a millimeter to 4 millimeters (Figure 4A, 4B), with both phases occasionally silicified (Figure 6). SEM/EDS analysis of the 19-AUS-19 thin section reveals reaction fronts where microcrystalline magnesite (blue, Figure 6) is overgrowing the discoidal dolomite that also contains embedded silicified grains. Microcrystalline magnesite is also observed to infill and surround the discoidal dolomite, as well as to aggregate with itself and with dolomite discs. Magnesite crystallites form sinuous, vermiform chains that anastomose throughout the aggregates (Figure 5D).

In the lower subsection (19-AUS-23, 19-AUS-22, 19-AUS-21), magnesite forms dense, bone-like, homogeneous, and mineralogically pure cauliflower-shaped nodules. The nodules are off-white to bright white in color and have a bulbous, hummocky surface with millimeter-scale pitting. The surfaces are further characterized by millimeter- to centimeter-scale reticular cracking (Figure 3E, 3F). The nodules have a light brown exterior veneer of clay or amorphous silica. Magnesite is present as well-formed rhombohedral crystals, which are largely devoid of inclusions. The magnesite matrix consists of fine-grained, equant magnesite (approximately 5-20 µm in diameter) that occurs as both non-interlocking and interlocking crystals suggesting moderate neomorphic recrystallization of primary magnesite (Figure 5A, 5B). Despite the macroscopically homogenous appearance of magnesite found in the lower subsection, there are small micronodules (approximately 10-20 µm) that are subtle yet consist of similarly fine-grained equant magnesite crystals displaying grain coarsening at the margins of the micronodules (Figure 5C). These relationships differ from those in the upper subsection wherein finer coatings of magnesite exist at the micronodules margins. The topmost sample from the lower subsection (19-AUS-23) contained rare detrital quartz, plagioclase, and feldspar as well as minor pore-lining chalcedony. This sample also indicated that magnesite was replacing plagioclase, following the plagioclase twinning through replacement and leaving moldic pores (Figure 6E, 6F), i.e., porosity created by a pre-existing constituent dissolving. In the deeper nodules (19-AUS-22, 19-AUS-21), microcrystalline magnesite was observed as equant, tightly packed grains with 100 micron- to millimeter-scale irregular pores that have dark halos. These colored halos may be discolored where plucked and/or soluble grains left pores through which fluids may have infiltrated, after the formation of the microcrystalline magnesite.

4 Formation and pedogenic alteration of a groundwater magnecrete

Observations across multiple spatial scales reveal that the quartz and arkosic sands present at the base of the profile are the result of Neogene/Quaternary fluvial deposition. These sediments were subject to diagenesis and chemical weathering to produce the authigenic clay and the Mg-carbonate at Kunwarara. Millimeter- to nanometer-scale observations of mineral grains associated with carbonate and secondary silica indicate multiple formation steps, which include dissolution and pre-existing carbonate reprecipitation as magnesite is found overgrowing dolomite and being overgrown by dolomite. These phases are records of both carbonate and silicate mineral weathering processes down to nanometer scales, as carbonate weathering produces pores during Mg dissolution. By contrast, silicates weather incongruently, producing alteration minerals and releasing dissolved Si species.

The Vertisol identified at Kunwarara is characterized by a series of soil horizons wherein multiple types of magnesite have co-developed with the surrounding sediments. There is an intimate relationship between the magnesite and clay, suggesting that both magnesite and clay are neoformed within the profile from weathering of arkosic sands via carbonation by Mg-rich fluids. The Kunwarara profile is a site of Mg accumulation where few primary Mg-bearing phases occur and magnesite increases in purity while authigenic silica phases decrease in abundance with depth. Pedogenic carbonate occurs overlying groundwater-formed magnesite that developed via downward alteration. Mg-carbonate is present as porous friable magnesite (top of the profile, Figure 2) and denser magnesite (bottom of the profile, Figure 2). Pore architecture controls the connectivity (i.e., permeability of the pore network) and a range of pore structures were observed. We report enhanced pore structures and permeability at the top of the profile (19-AUS-19) and reduced pore sizes and predominantly nano- to microscale intercrystalline porosity deeper belowground (19-AUS-24 to 19-AUS-21, Figure 2).

Our petrographic and spectroscopic results suggest that magnesite precipitates as Mg^{2+}- and CO_3^{2-} - rich groundwaters move upward through the soil profile, with magnesite recrystallizing and becoming more pure at the base of the profile with each precipitation event. At the top of the profile, magnesite overgrows dolomite and fills voids left by dissolving clay. Dolomite may be formed late in the upward paragenesis, as initially $Mg^{+2}_{(aq)}$-rich groundwaters became progressively enriched in $Ca^{+2}_{(aq)}$. Aqueous $Ca^{+2}_{(aq)}$ could have reacted with early formed magnesite or Mg-rich groundwater, producing late-stage dolomite. In addition, aqueous $Na^{+1}_{(aq)}$ and $K^{+1}_{(aq)}$ could have combined with dissolved H_4SiO_4 produced by the etching and dissolution of detrital quartz to produce the authigenic clay minerals observed. Authigenic aluminous clays may also have formed in situ by the incongruent dissolution of feldspars. The discoidal dolomite texture could be a result of precipitating dolomite from an aqueous hydromagnesite solution that was enriched in Ca from surficial sources.

Fluctuating fluid conditions are inferred from the aforementioned petrographic observations indicating that the magnesite becomes altered through dissolution and recrystallization processes (Figure 5), which are hypothesized to be ultimately driven by fluctuations in the water table that impart variations in soil pH, changing oxygen conditions, and the availability of reactive mineral or organic phases (Fischel et al., 2023; Power et al., 2017). The presence and development of variably sized Mg-carbonate glaebules within Mg-carbonate

nodules would also support fluctuating fluid conditions (Roy Brewer, 1964). These hydrologic changes result in variations in magnesite crystal morphology, size, and chemical composition across different soil horizons as well as in the accessory phases, which are observed (Figure 3, Figure 6, Figure 7).

4.1 Evolution of a Mg-carbonate-bearing and vertisol capped sedimentary succession

The dark smectite soil horizon may have multiple roles in the evolution of the precipitating phases within the underlying Kunwawara sedimentary succession. A top-down hypothesis for the genesis of the overlying clay layer made up of predominantly shrink-swell clays has developed atop the magnesite and sands is the weathering of arkosic sand by meteoric surface waters, which produces authigenic clays and dissolves the underlying magnesite. When the clays swell, they may act as a capping layer to the lower lithologies. This cap could limit the disintegration of the friable magnesite at the top of the profile and enable enhanced 'hotspot' biogeochemical activity within the vadose zone, allowing pCO_2 to build up then become a destructive agent to magnesite. Or, alternatively, the cap could preserve the initial conditions and alteration extent because the clay unit caps the dolomite and magnesite units, thus limiting precipitation and fluid flow. A second hypothesis for the role of the overlying smectite layer is that it supplies particulate or dissolved organic matter to the subsurface, allowing pedogenic solutions to infiltrate downwards when the clays shrink and supporting the development of magnesite at depth because organic surfaces have been shown to facilitate and potentially control the formation of magnesite at low temperatures (Power et al., 2017, 2019). A third hypothesis is that the smectite soil formed as ascending groundwaters evaporated, dissolving the arkosic sand matrix, precipitating magnesite, and carrying Si phases to shallower depths. Salinity changes have major impacts on the swell ability of shrink-swell clays, their exchange capacity (Carroll & Starkey, 1958), and the molecular kinetics of clay surfaces (Cama & Ganor, 2015). Figure 7 and Table S4 illustrate the geochemical relationship between the magnesite and clays. Rare earth element data reported by Swindle et al. (2025) indicate that only the shallowest magnesite shows elemental signatures of the host sediments, while deeper samples show a flat, chondritic profile consistent with ultramafic rock-derived fluids. These findings indicate that the Mg-rich, ultramafic-derived groundwaters repeatedly recrystallized the deepest, most mature magnesites. The least mature, initial magnesite and dolomite at the top of the profile derives largely from the residue of the dissolving sediments. These findings also support the third hypothesis for the origin of the swelling clays in the overlying vertisol: upward-migrating groundwater dissolves arkosic sand and precipitates magnesite, followed by dolomite and silica phases enabled by accumulation of solutes as the sand dissolves.

Vertical mobility and development in the vertisol over differing timescales could be induced by an interplay of wet-dry conditions driven by seasonal fluctuations as well as more intense climatic regime changes. Vertisols that contain abundant shrink-swell clay develop in tropical and subtropical climates with pronounced wet and dry seasons. Pronounced wet and dry seasons, in turn, provide the opportunity for seasonal modification of the local groundwater that provides insight into the formation of the Kunwarara vertisols hosting accumulated magnesite. The combination of multiple authigenic mineral phases and evidence for repeated

episodes of mineral dissolution-reprecipitation within the Kunwarara magnesite nodules is consistent with formation from episodic and recurring groundwater upwelling. Figure 8 provides a summary of potential environments of accumulation and diagenesis of magnesite within the Kunwarara vertisol. In this scenario, the composition of the local groundwaters, dominated by bicarbonate and magnesium, changes through seasonal variations in evaporation, evapotranspiration, and Ca-rich surface water influx.

The complex petrographic fabrics within the Kunwarara magnesite nodules suggest that the magnesite itself has undergone repeated episodes of wetting/drying and dissolution/precipitation. Evidence for magnesite dehydration is most easily observed on the surfaces of nodules, which commonly show a 0.5 centimeter-scale polygonal pattern of cracks (Figure 3). These cracks can narrow with depth or retain the same width several millimeters into the nodule. Such polygonal cracking is indicative of contraction with water loss, suggesting potential dehydration of an originally hydrated $MgCO_3$ phase or the nodules growing/coalescing, or even dissolving. The circumgranular fractures throughout the nodular fabric is also consistent with soil motion during growth (i.e. compaction, clay shrink/swell, root bioturbation, etc.) (Alonso-Zarza & Wright, 2010; Wright, 2007) and plasmic zone textures (Wright, 1982). Apparent termination of equal-width cracks at an equivalent depth in the nodule may also indicate dehydration of just the most recent material added to the nodule during growth.

Microscopy reveals petrographic evidence of pedogenic overprinting affecting the Mg-clay minerals as well as the carbonates. Within the Mg-clays, replacement by silica (quartz, chalcedony) and carbonates (dolomite and magnesite) is common. We also observe a homogenization of the magnesite textures into a laminar texture (19-AUS-22), which may have occurred during the diagenetic compaction process (Kadir et al., 2018) or as a result of prior microbial activity in-situ (Eren et al., 2018). At Kunwarara, the multiple clay phases are interpreted to be authigenically formed. Laboratory experiments have demonstrated low-temperature magnesite precipitation occurring with fluctuating pH conditions (Hobbs & Xu, 2020) or with densely packed active carbon sites (i.e., available carboxyl groups), which bind yet also dehydrate Mg^{2+} ions from solutions (Power et al., 2017). Carbon speciation can influence the process of magnesite precipitation as well as the habit the magnesite acquires, both of which may be occurring within this profile. Montes-Hernandez *et al.* (2020) indicated that functionalized organic groups can reduce the energetic barriers during magnesite nucleation.

The magnesite accumulation at Kunwarara shares many features with groundwater calcretes in other terrestrial settings. The location of the magnecrete horizon reflects the balance between downward carbonate redistribution by the leaching of dissolved carbonate in a percolating acidic soil solution, and accumulation resulting from capillary action from Mg-rich alkaline groundwater near the top of the water table moving upwards. The location of this zone is controlled by the extent of the wetting front following rainfall events (Goudie, 1983). Lateral transfers of carbonate-rich groundwater result in carbonate mineral accumulation displaced from the site of weathering (Arakel, 1986; Bachman & Machette, 1977; Goudie, 1983), so carbonate precipitation occurs by replacing sediments near the groundwater table (Alonso-Zarza, 2003; McLaren & Gardner, 2004; Nash & McLaren, 2003).

Water survey data (McNeil & Raymond, 2013) and our morphological interpretations suggest that this profile is a moderately alkaline weak-leaching environment wherein Si may be sourced from the detrital arkosic sands that predate the formation of magnesite. Detrital plagioclase or exogenous sources encountered during the transport of rainwater within the catchment, infiltrating into the sediment profile may source the Ca found within the top of the profile, which has undergone multiple aqueous alteration events. Under alkaline aqueous conditions, Mg (as aqueous Mg^{+2}) and Si (as H_4SiO_4) are soluble and high CO_3^{-2} concentrations are possible. Other Australian localities have also reported an increase in Mg content of Ca-Mg carbonates with depth (McQueen et al., 1999; Milnes & Hutton, 1983).

5 Linkages to the Margin Unit, Jezero crater, Mars

Orbital and rover-based observations have revealed that the Margin Unit of Jezero crater is a significant, widespread Martian deposit of carbonate with a Mg-carbonate composition (Horgan et al., 2020; Tarnas et al., 2021) and the potential to record past water-rock interactions and signs of ancient life. Recent in-situ rover observations in the Margin Unit have identified that this unit has moderately to poorly sorted medium to coarse-grained rock (*Pelican Point, Mandu Wall area*) that is layered in outcrop (Farley & Stack, 2025). In these rocks, Mg-carbonate and silica are present as both coatings and cements with varying hydration states. Interpretations for this outcrop suggest a silica-cemented medium to coarse sandstone that underwent aqueous alteration (Farley & Stack, 2025). These in situ observations combined with the collection of two drill-cores for sample-return reveal the importance of studying large-scale Mg carbonate deposits (i.e., Kunwarara, QLD, Australia) as a useful Mars analogs.

While the primary mineralogy of the sand grains differs between those detected in Jezero crater (basaltic to ultramafic) and Kunwarara (felsic), the two localities exhibit similar sand grain sizes and accumulations of Mg-carbonate minerals associated with authigenic phyllosilicates in sedimentary deposits (Farley & Stack, 2025), indicating that some of the Jezero Mg-carbonate may have formed from low-temperature processes such as pedogenesis or groundwater alteration. Thus, inferences from the mineralogy and textural relationships preserved in the Kunwarara sediment profile (Figure 8) may have significant implications for understanding the chemical composition, formation, water-rock interactions, and geologic history of the Margin Unit within Jezero crater from compelling parallels between the two localities. Overall, this study provides useful insights, though analog sites cannot exactly replicate the complex and unique conditions found on Mars. Future investigations might focus on expanding the range and simulations conducted at Kunwarara to encompass a broader array of Martian conditions and rover-like analyses for improved comparative study. This study supports that magnecretes as well as calcretes (Alonso-Zarza & Silva, 2002) develop as a result of an interplay of pedogenesis, groundwater precipitation, and episodic alteration that are visible in the depth horizons as well as down to the centimeter to micrometer scales. This work expands the environments and formation mechanisms that could be responsible for widespread Mg-carbonate orbital detections and the search for possible biosignatures that might be preserved in Mg-carbonates on Mars.

6 Conclusions

The Kunwarara Vertisol records various stages of magnesite formation and alteration. Identified microtextures and mineralogy within both the magnesite and the matrix track the timing, intensity, and relative relationships of the presented processes – predominantly magnesite authigenesis and diagenesis (i.e. precipitation-dissolution) through dynamic eluvial-illuvial activity occurring in the matrix. Textural evidence indicates that rising, ultramafic-derived groundwaters precipitate in the capillary zone of alluvial sediments that have developed a vertisol profile after undergoing multiple stages of precipitation-dissolution. The elemental constituents are sourced from weathering of the Princhester Serpentinite and subsurface lateral flow of groundwater enriched in magnesium and bicarbonate. Our analyses revealed evidence of upward movement of groundwater into the Vertisol profile and movement within the vertical profile.

Moreover, within this system, the oldest, most evolved diagenetic magnesite horizon has developed and been preserved at the base of the profile as a Mg-carbonate cement. It forms dense nodules with little to no macroscopic pore-space and has an intimate formational relationship with Si that may also aid in its preservation. Petrographic results indicate that the dissolution of arkosic sands was coupled with precipitation of secondary silica and clays. A pedogenic dolomite-rich horizon above the magnesites developed as the fluid previously rich in magnesium and bicarbonate evolved toward a more Ca-rich composition because magnesite and Mg-clay phases remove magnesium, while the dissolution of detrital plagioclase releases calcium. These precipitated Mg-carbonate phases, containing Mg-rich dolomite and magnesite, undergo greater destruction and alteration due to infiltrating surficial waters.

This study documents and elucidates the processes that have led to the formation and preservation of a unique sediment-hosted magnecrete. These findings have major implications for understanding the Mg-carbonate bearing units of Jezero crater and in other localities on Mars. More generally, they may also preserve evidence of Mars' past water cycle, offering valuable hydrologic insights that could be returned to Earth through a potential Mars Sample Return Mission.

Acknowledgments

Support for E.L. Cardarelli was provided by NASA grant 80NM0018D0004 through the Jet Propulsion Laboratory, California Institute of Technology. This work was supported by the Simons Foundation grant #668346 awarded to J. Grotzinger and the National Science Foundation Graduate Research Fellowship grant (DGE-1745301) awarded to C. Swindle.

References

Alonso-Zarza, A.M., & Silva, P. G. (2002). Quaternary laminar calcretes with bee nests: evidences of small-scale climatic fluctuations, Eastern Canary Islands, Spain. *Palaeogeography, Palaeoclimatology, Palaeoecology*, *178*(1–2), 119–135. https://doi.org/10.1016/S0031-0182(01)00405-9

Alonso-Zarza, A.M., & Wright, V. P. (2010). Chapter 5 Calcretes. In *Developments in Sedimentology* (Vol. 61, pp. 225–267). Elsevier. https://doi.org/10.1016/S0070-4571(09)06105-6

Alonso-Zarza, Ana M. (2003). Palaeoenvironmental significance of palustrine carbonates and calcretes in the geological record. *Earth-Science Reviews*, *60*(3–4), 261–298. https://doi.org/10.1016/S0012-8252(02)00106-X

Arakel, A. V. (1986). Evolution of calcrete in palaeodrainages of the Lake Napperby area, Central Australia. *Palaeogeography, Palaeoclimatology, Palaeoecology*, *54*(1–4), 283–303. https://doi.org/10.1016/0031-0182(86)90129-X

Bachman, G. O., & Machette, M. N. (1977). *Calcic soils and calcretes in the southwestern United States*. US Geological Survey,.

Batianoff, G., & Singh, S. (2001). Central Queensland serpentine landforms, plant ecology and endemism. *South African Journal of Science*, *97*(11), 495–500.

Bohor, B. F., & Hughes, R. E. (1971). Scanning Electron Microscopy of Clays and Clay Minerals. *Clays and Clay Minerals*, *19*(1), 49–54. https://doi.org/10.1346/CCMN.1971.0190105

Braithwaite and Zedef. (1996). Hydromagnesite Stromatolites and Sediments in an Alkaline Lake, Salda Golu, Turkey. *SEPM Journal of Sedimentary Research*, *Vol. 66*. https://doi.org/10.1306/D426845F-2B26-11D7-8648000102C1865D

Brewer, R., & Sleeman, J. R. (1964). GLAEBULES: THEIR DEFINITION, CLASSIFICATION AND INTERPRETATION. *Journal of Soil Science*, *15*(1), 66–78. https://doi.org/10.1111/j.1365-2389.1964.tb00245.x

Brewer, Roy. (1964). Fabric and mineral analysis of soils.

Bruce, M. C., & Niu, Y. (2000). Evidence for Palaeozoic magmatism recorded in the Late Neoproterozoic Marlborough ophiolite, New England Fold Belt, central Queensland. *Australian Journal of Earth Sciences*, *47*(6), 1065–1076. https://doi.org/10.1046/j.1440-0952.2000.00834.x

Cama, J., & Ganor, J. (2015). Dissolution Kinetics of Clay Minerals. In *Developments in Clay Science* (Vol. 6, pp. 101–153). Elsevier. https://doi.org/10.1016/B978-0-08-100027-4.00004-8

Carroll, D., & Starkey, H. C. (1958). Effect of Sea-Water on Clay Minerals. *Clays and Clay Minerals (National Conference on Clays and Clay Minerals)*, *7*, 80–101. https://doi.org/10.1346/CCMN.1958.0070103

Catling, D. C. (1999). A chemical model for evaporites on early Mars: Possible sedimentary tracers of the early climate and implications for exploration. *Journal of Geophysical Research: Planets*, *104*(E7), 16453–16469. https://doi.org/10.1029/1998JE001020

Ehlmann, B. L., Mustard, J. F., Murchie, S. L., Poulet, F., Bishop, J. L., Brown, A. J., et al. (2008). Orbital Identification of Carbonate-Bearing Rocks on Mars. *Science*, *322*(5909), 1828–1832. https://doi.org/10.1126/science.1164759

Eren, M., Kaplan, M. Y., Kadir, S., & Kapur, S. (2018). Biogenic (β-fabric) features in the hard laminated crusts of the Mersin and Adana regions, southern Turkey and the role of soil

organisms in the formation of the calcrete profiles. *CATENA*, *168*, 34–46. https://doi.org/10.1016/j.catena.2017.12.021

Evans, P. R., & Roberts, J. (1979). Evolution of central eastern Australia during the late Palaeozoic and early Mesozoic. *Journal of the Geological Society of Australia*, *26*(7–8), 325–340. https://doi.org/10.1080/00167617908729100

Falk, E. S., & Kelemen, P. B. (2015). Geochemistry and petrology of listvenite in the Samail ophiolite, Sultanate of Oman: Complete carbonation of peridotite during ophiolite emplacement. *Geochimica et Cosmochimica Acta*, *160*, 70–90. https://doi.org/10.1016/j.gca.2015.03.014

Fischel, M. H. H., Clarke, C. E., & Sparks, D. L. (2023). Synchrotron resolved microscale and bulk mineralogy in manganese-rich soils and associated pedogenic concretions. *Geoderma*, *430*, 116305. https://doi.org/10.1016/j.geoderma.2022.116305

Forster, B., & Baker, D. (1997). Characterisation of the serpentinite soils of central Queensland, Australia. *Écologie Des Milieux Sur Roches Ultramafiques et Sur Sols Métallifères. Documents Scientifiques et Techniques No. III/2'.(Eds T Jaffré T, RD Reeves, T Becquer) Pp*, 27–37.

Foster, L., Eggleton, R. A., & Roach, I. (2002). The Marlborough nickel laterite deposits. In *Presented at the Regolith and Landscapes in Eastern Australia Conference, CRC LEME* (Vol. 1, pp. 33–36). Citeseer.

García Del Real, P., & Vishal, V. (2016). Mineral Carbonation in Ultramafic and Basaltic Rocks. In V. Vishal & T. N. Singh (Eds.), *Geologic Carbon Sequestration* (pp. 213–229). Cham: Springer International Publishing. https://doi.org/10.1007/978-3-319-27019-7_11

Goudie, A. S. (1983). Calcrete., 93–131.

Hobbs, F. W. C., & Xu, H. (2020). Magnesite formation through temperature and pH cycling as a proxy for lagoon and playa paleoenvironments. *Geochimica et Cosmochimica Acta*, *269*, 101–116. https://doi.org/10.1016/j.gca.2019.10.014

Horgan, B. H. N., Anderson, R. B., Dromart, G., Amador, E. S., & Rice, M. S. (2020). The mineral diversity of Jezero crater: Evidence for possible lacustrine carbonates on Mars. *Icarus*, *339*, 113526. https://doi.org/10.1016/j.icarus.2019.113526

K. Farley, & K. Stack. (n.d.). Mars 2020 Initial Reports Volume 4. https://doi.org/10.17189/MZX3-K371

Kadir, S., Eren, M., Külah, T., Erkoyun, H., Huggett, J., & Önalgil, N. (2018). Genesis of palygorskite and calcretes in Pliocene Eskişehir Basin, west central Anatolia, Turkey. *CATENA*, *168*, 62–78. https://doi.org/10.1016/j.catena.2017.09.027

Kalucha, H., Broz, A., Randazzo, N., Aramendia, J., Madariaga, J. M., Garczynski, B., et al. (2024). Probable Concretions Observed in the Shenandoah Formation of Jezero Crater, Mars and Comparison With Terrestrial Analogs. *Journal of Geophysical Research: Planets*, *129*(8), e2023JE008138. https://doi.org/10.1029/2023JE008138

Kaplan, M., Eren, M., KadïR, S., Kapur, S., & Huggett, J. (2014). A microscopic approach to the pedogenic formation of palygorskite associated with Quaternary calcretes of the Adana area, southern Turkey. *TURKISH JOURNAL OF EARTH SCIENCES*, *23*, 559–574. https://doi.org/10.3906/yer-1401-3

Lin, H. (2011). Three Principles of Soil Change and Pedogenesis in Time and Space. *Soil Science Society of America Journal*, *75*(6), 2049–2070. https://doi.org/10.2136/sssaj2011.0130

Lumsden. (1988). Characteristics of Deep-Marine Dolomite. *SEPM Journal of Sedimentary Research*, *Vol. 58*. https://doi.org/10.1306/212F8EEF-2B24-11D7-8648000102C1865D

Mavromatis, V., Power, I. M., Harrison, A. L., Beinlich, A., Dipple, G. M., & Bénézeth, P. (2021). Mechanisms controlling the Mg isotope composition of hydromagnesite-magnesite playas near Atlin, British Columbia, Canada. *Chemical Geology*, *579*, 120325. https://doi.org/10.1016/j.chemgeo.2021.120325

McLaren, S., & Gardner, R. (2004). Late Quaternary vadose carbonate diagenesis in coastal and desert dune and beach sands: is there a palaeoclimatic signal? *Earth Surface Processes and Landforms*, *29*(12), 1441–1458. https://doi.org/10.1002/esp.1132

McNeil, V. H., & Raymond, M. A. A. (2013). Mapping regional groundwater chemistry zones in the Fitzroy Basin, using statistical and conceptual methods. *The Proceedings of the Royal Society of Queensland*, *118*, 37–61. https://doi.org/10.5962/p.357778

McQueen, K. G., Hill, S. M., & Foster, K. A. (1999). The nature and distribution of regolith carbonate accumulations in southeastern Australia and their potential as a sampling medium in geochemical exploration. *Journal of Geochemical Exploration*, *67*(1–3), 67–82. https://doi.org/10.1016/S0375-6742(99)00071-0

Milburn, D., & Wilcock, S. (1998). Kunwarara magnesite deposit. *Geol Aust Papua New Guinean Min Depos, Australasian Inst Min and Metall Monogr*, *22*, 815–818.

Milnes, A., & Hutton, J. T. (1983). Calcretes in Australia - a review (pp. 119–162).

Mittlefehldt, D. W. (1994). ALH84001, a cumulate orthopyroxenite member of the martian meteorite clan. *Meteoritics*, *29*(2), 214–221. https://doi.org/10.1111/j.1945-5100.1994.tb00673.x

Murray, C. G. (2007). Devonian supra-subduction zone setting for the Princhester and Northumberland Serpentinites: implications for the tectonic evolution of the northern New England Orogen. *Australian Journal of Earth Sciences*, *54*(7), 899–925. https://doi.org/10.1080/08120090701392747

Nash, D. J., & McLaren, S. J. (2003). Kalahari valley calcretes: their nature, origins, and environmental significance. *Quaternary International*, *111*(1), 3–22. https://doi.org/10.1016/S1040-6182(03)00011-9

Oskierski, H. C., Bailey, J. G., Kennedy, E. M., Jacobsen, G., Ashley, P. M., & Dlugogorski, B. Z. (2013). Formation of weathering-derived magnesite deposits in the New England Orogen, New South Wales, Australia: Implications from mineralogy, geochemistry and genesis of the Attunga magnesite deposit. *Mineralium Deposita*, *48*(4), 525–541. https://doi.org/10.1007/s00126-012-0440-5

Oskierski, H. C., Beinlich, A., Mavromatis, V., Altarawneh, M., & Dlugogorski, B. Z. (2019). Mg isotope fractionation during continental weathering and low temperature carbonation of ultramafic rocks. *Geochimica et Cosmochimica Acta*, *262*, 60–77. https://doi.org/10.1016/j.gca.2019.07.019

Paul Wright, V. (1982). Calcrete palaeosols from the lower carboniferous llanelly formation, South Wales. *Sedimentary Geology*, *33*(1), 1–33. https://doi.org/10.1016/0037-0738(82)90025-2

Pohl, W. (1989). Comparative geology of magnesite deposits and occurrences. *Monogr. Ser. Mineral Deposits*, *28*, 1–13.

Power, I. M., Kenward, P. A., Dipple, G. M., & Raudsepp, M. (2017). Room Temperature Magnesite Precipitation. *Crystal Growth & Design*, *17*(11), 5652–5659. https://doi.org/10.1021/acs.cgd.7b00311

Power, I. M., Harrison, A. L., Dipple, G. M., Wilson, S., Barker, S. L. L., & Fallon, S. J. (2019). Magnesite formation in playa environments near Atlin, British Columbia, Canada. *Geochimica et Cosmochimica Acta*, *255*, 1–24. https://doi.org/10.1016/j.gca.2019.04.008

Raudsepp, M. J., Wilson, S., Zeyen, N., Arizaleta, M. L., & Power, I. M. (2024). Magnesite everywhere: Formation of carbonates in the alkaline lakes and playas of the Cariboo Plateau, British Columbia, Canada. *Chemical Geology*, *648*, 121951. https://doi.org/10.1016/j.chemgeo.2024.121951

Scheller, E. L., Swindle, C., Grotzinger, J., Barnhart, H., Bhattacharjee, S., Ehlmann, B. L., et al. (2021). Formation of Magnesium Carbonates on Earth and Implications for Mars. *Journal of Geophysical Research: Planets*, *126*(7), e2021JE006828. https://doi.org/10.1029/2021JE006828

Scheller, E. L., Razzell Hollis, J., Cardarelli, E. L., Steele, A., Beegle, L. W., Bhartia, R., et al. (2022). Aqueous alteration processes in Jezero crater, Mars—implications for organic geochemistry. *Science*, *378*(6624), 1105–1110. https://doi.org/10.1126/science.abo5204

Steele, A., Benning, L. G., Wirth, R., Schreiber, A., Araki, T., McCubbin, F. M., et al. (2022). Organic synthesis associated with serpentinization and carbonation on early Mars. *Science*, *375*(6577), 172–177. https://doi.org/10.1126/science.abg7905

Swindle, C., Vasconcelos, P., Dimarco, Z., Dalleska, N., Nguyen, A., Cardarelli, E., et al. (2025). Elemental signatures of metamorphic, diagenetic, and pedogenic magnesites from Central Queensland, Australia. *Chemical Geology*, *695*, 123068. https://doi.org/10.1016/j.chemgeo.2025.123068

Swindle, C., Vasconcelos, P., Dalleska, N., Cardarelli, E., Bhattacharjee, S., Dimarco, Z., et al. (2025). Trace element compositions and redox shifts preserved in magnesites, sediments and soils from the Kunwarara magnesite mine. *Applied Geochemistry*, *191*, 106494. https://doi.org/10.1016/j.apgeochem.2025.106494

Tarnas, J. D., Stack, K. M., Parente, M., Koeppel, A. H. D., Mustard, J. F., Moore, K. R., et al. (2021). Characteristics, Origins, and Biosignature Preservation Potential of Carbonate-Bearing Rocks Within and Outside of Jezero Crater. *Journal of Geophysical Research: Planets*, *126*(11), e2021JE006898. https://doi.org/10.1029/2021JE006898

Valdespino-Castillo, P. M., Águila, B., Torres-Huesca, J., Centeno, C. M., Martínez-Díaz, J., Reyes-Salas, M., et al. (2022). Microbialites: Diversity Hotspots in the Mexican Plateau. In J. Alcocer (Ed.), *Lake Alchichica Limnology* (pp. 375–390). Cham: Springer International Publishing. https://doi.org/10.1007/978-3-030-79096-7_22

Wright, V. P. (2007). Calcrete. In D. J. Nash & S. J. McLaren (Eds.), *Geochemical Sediments and Landscapes* (1st ed., pp. 10–45). Wiley. https://doi.org/10.1002/9780470712917.ch2

Zeissink, H. E. (1969). The mineralogy and geochemistry of a nickeliferous laterite profile (Greenvale, Queensland, Australia). *Mineralium Deposita*, *4*(2). https://doi.org/10.1007/BF00208049

Figures

Figure 1. Geologic and pedogenic context of Kunwarara, Queensland, Australia. Modified from the GSQ 2012 geologic map, ASTER GDEM v3, and CSIRO Digital Atlas of Australian Soils. **(A)** The geologic context of Kunwarara, Queensland, Australia is presented at the regional scale **(A)** and within the broader box of the broader Australia context inset map in red. **(B)** Pedologic context of greater Kunwarara area with soil units is labeled. The pedologic unit hosting the magnesite and sediment matrix investigated is indicated in dark grey, with the locality sampled denoted with a red diamond.

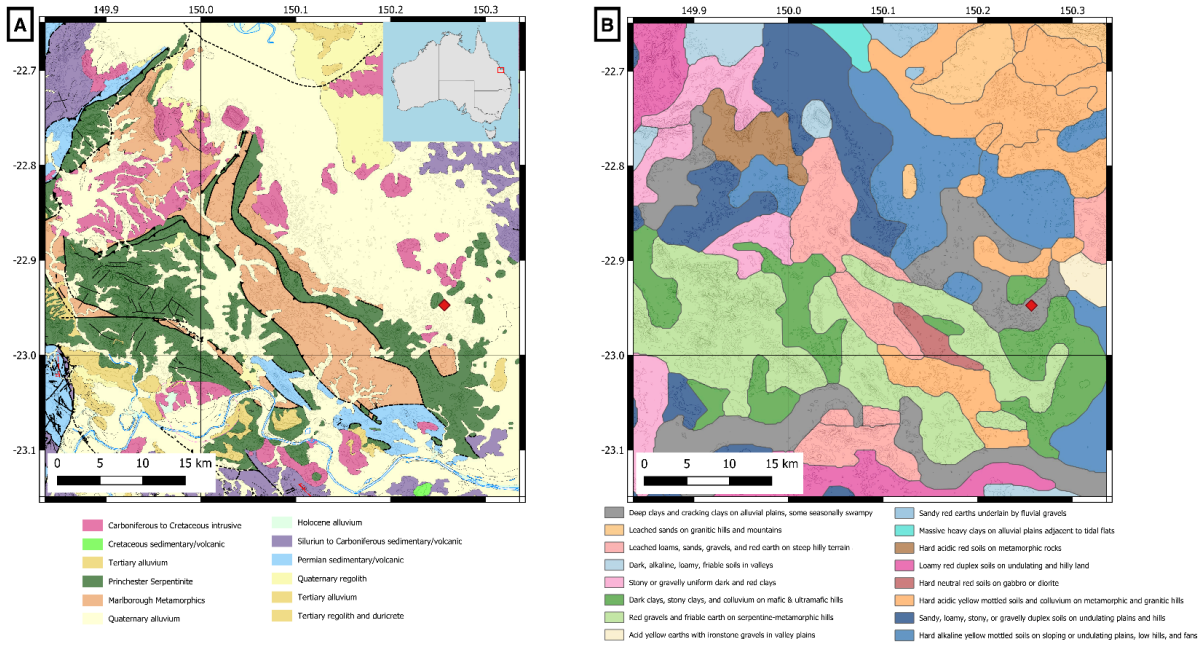

Figure 2. Field context of Kunwarara, Queensland, Australia. Field photos of Mg deposits in an exemplary vertisol **(A, B)** in Kunwarara where mining activities in the area have created terraces **(C-E)**. The magnesites presented herein are formed when the arkosic sands undergoes partial replacement by nodular magnesite which forms from precipitation from Mg-rich groundwater. Fewer precipitation cycle at the top of the profile in concert with dissolution cycles incurred by rainwater infiltration produce weakly lithified magnesite nodules **(A, B)**. Many precipitation cycles produce a magnesite cement **(E)** at depth wherein magnesite spires develop through evaporation and pure Mg-carbonate nodules are also hosted.

Figure 3. Carbonate nodule texture plates. Color-balanced images of magnesite hand samples with a 10 mm scale bar are arranged by position in the vertical profile beginning with 19-AUS-19 **(A, B)** at the top followed by 19-AUS-24 **(C, D)**, 19-AUS-23 **(E, F)**, 19-AUS-22 **(G, H)**, and 19-AUS-21 **(I, J)** at the bottom.

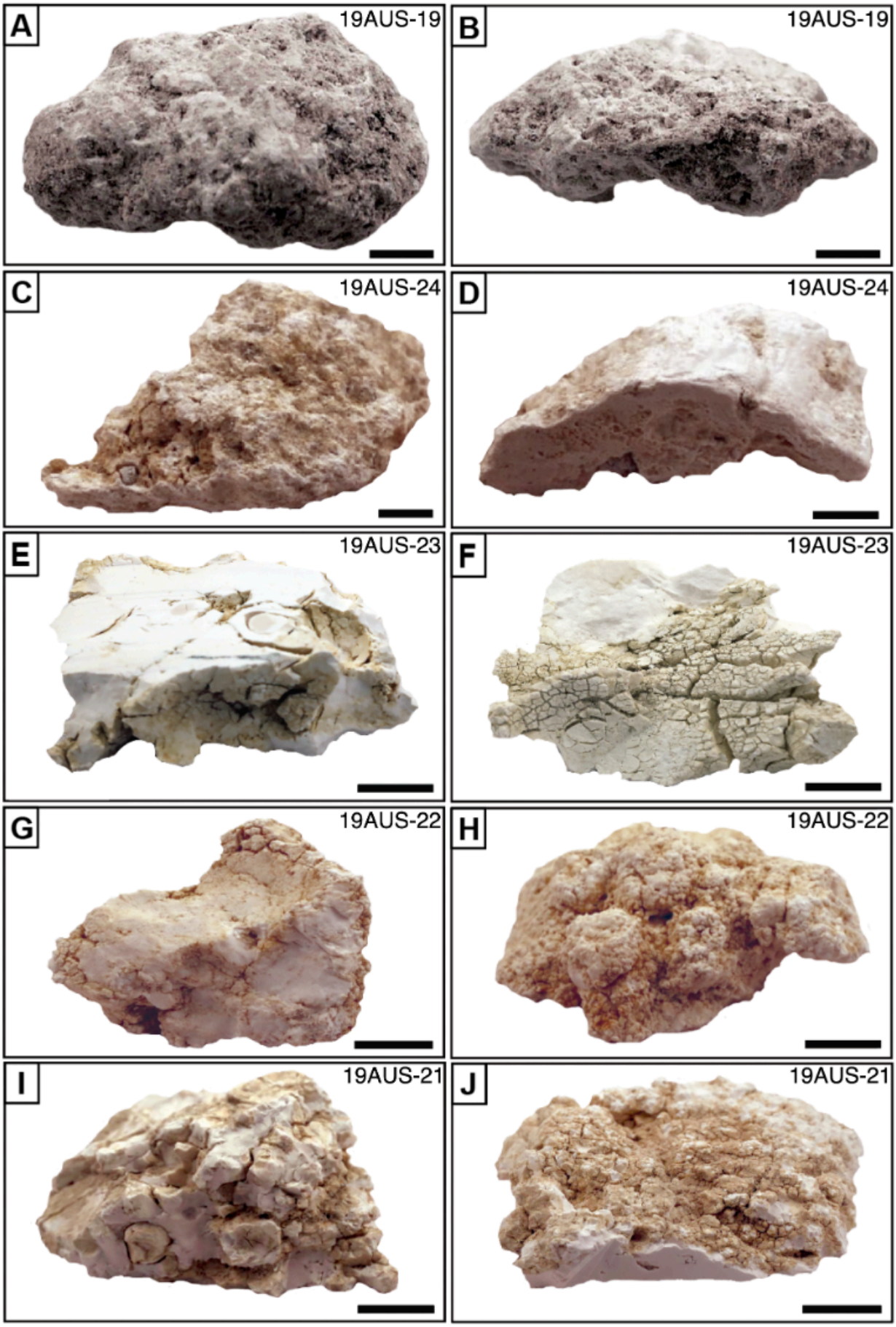
A
19AUS-19
B
19AUS-19
C
19AUS-24
D
19AUS-24
E
19AUS-23
F
19AUS-23
G
19AUS-22
H
19AUS-22
I
19AUS-21
J
19AUS-21

Figure 4. Carbonate thin section plates (27 mm x 42 mm) and x-ray fluorescence billet maps. Samples are arranged by position in the vertical profile beginning with 19-AUS-19 **(A, B)** at the top followed by 19-AUS-24 **(C, D)**, 19-AUS-23 **(E, F)**, 19-AUS-22 **(G, H)**, and 19-AUS-21 **(I, J)** at the bottom. Thin sections are in the left column and their corresponding x-ray fluorescence billet maps are in the right column with elemental legends in the lower left of each map.

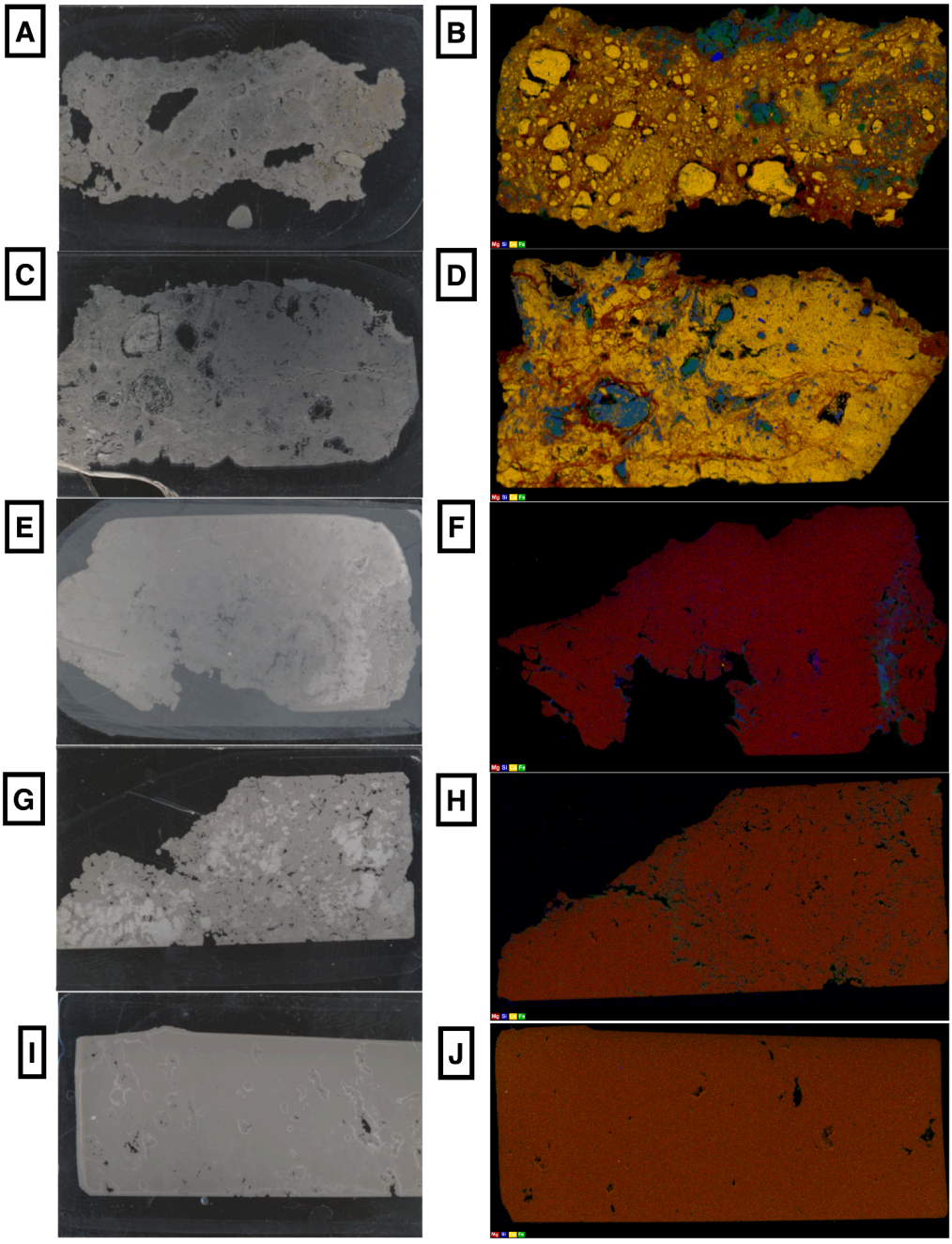

Figure 5. Photomicrography of textures and relationships to other phases. Samples are arranged by position in the vertical profile beginning with 19-AUS-19 **(A, B, C)** at the top followed by 19-AUS-24 **(D, E)**, 19-AUS-23 **(F, G)**, 19-AUS-22 **(H)**, and 19-AUS-21 **(I, J)** at the bottom.

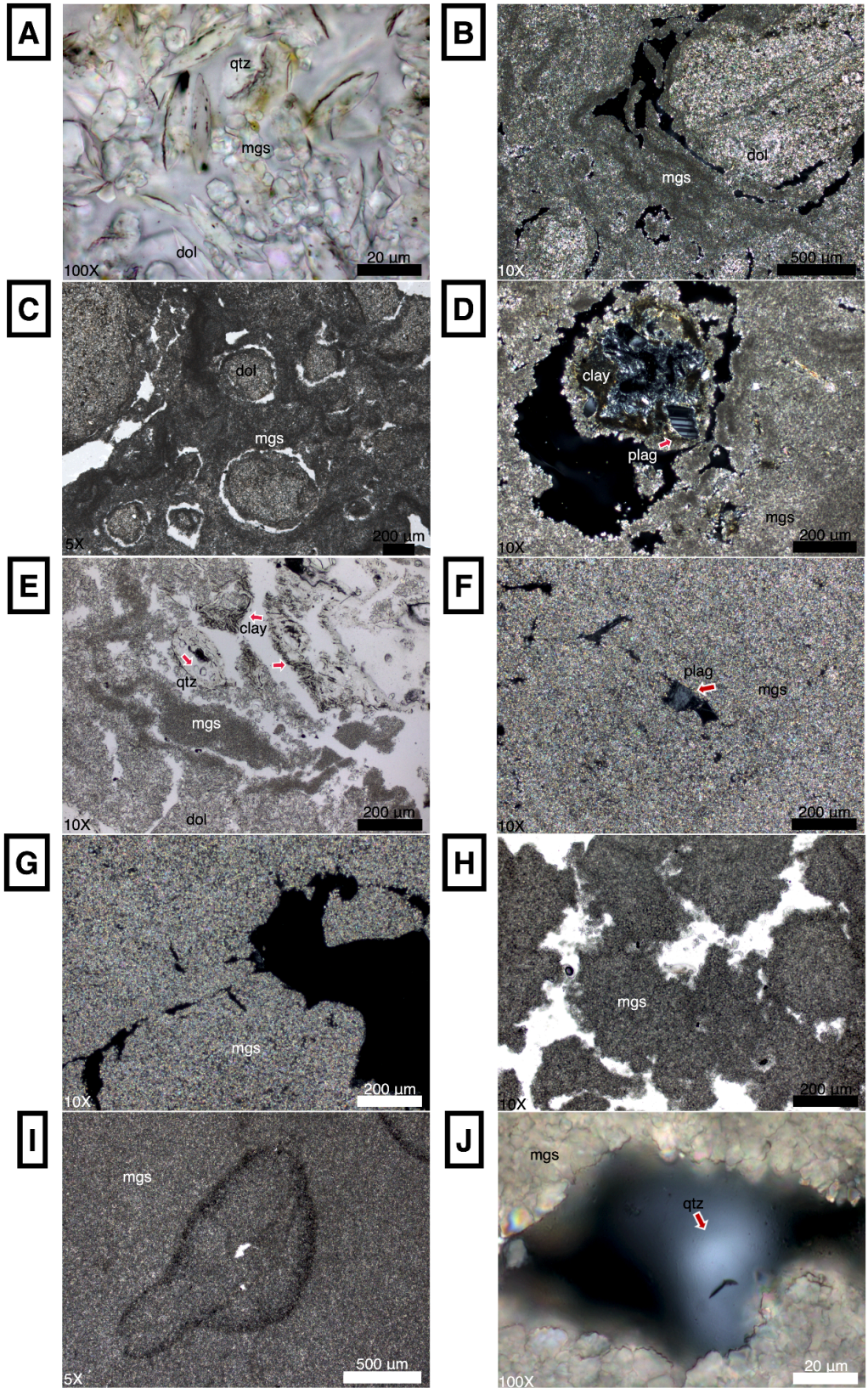
A
qtz
mgs
dol
100X
20 µm
B
dol
mgs
10X
500 µm
C
dol
mgs
5X
200 µm
D
clay
plag
mgs
10X
200 µm
E
clay
qtz
mgs
10X
dol
200 µm
F
plag
mgs
10X
200 µm
G
mgs
10X
200 µm
H
mgs
10X
200 µm
I
mgs
5X
500 µm
J
mgs
qtz
100X
20 µm

Figure 6. SEM plate of magnesite – dolomite – silica textures and relationships. Magnesite (blue), dolomite (pink/orange), and silica (green) phases in multiple samples are arranged by position in the vertical profile beginning with 19-AUS-19 **(A, B, C)** in the top row are contrasted to the base of the profile 19-AUS-21 **(D, E)** where silica infills voids of the cryptocrystalline magnesite cement as colloform chalcedony (D) and where silica-bearing phases become entrained in the magnesite cement **(E)**. At intermediate depths (19-AUS-24), discoidal dolomite is embedded into the microcrystalline magnesite and both phases are silicified **(F)**.

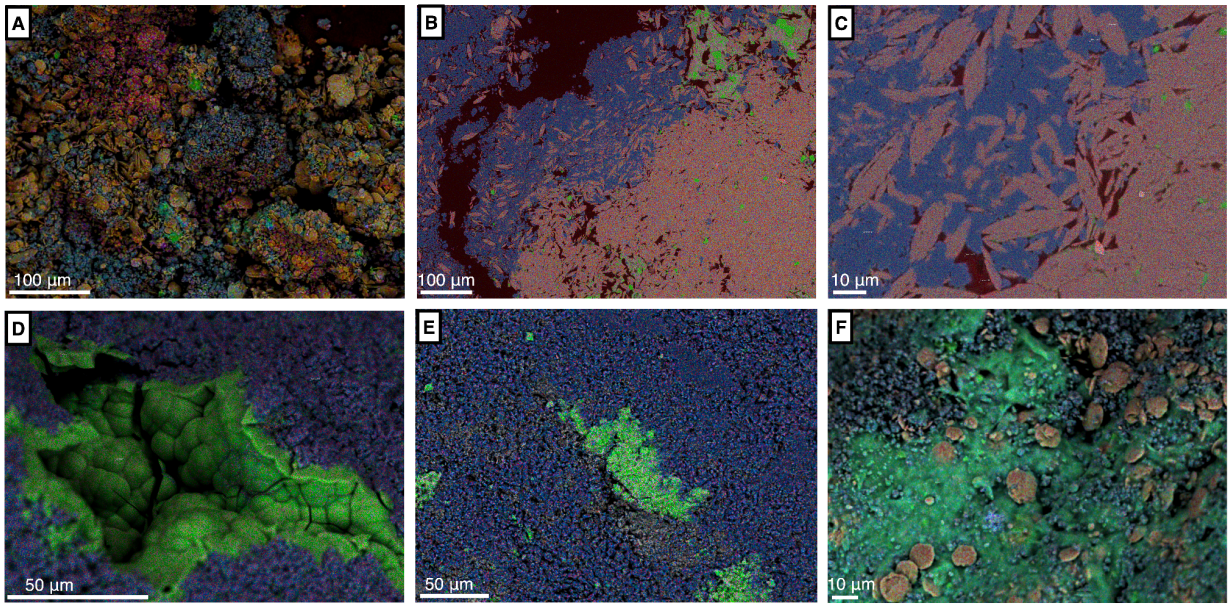

Figure 7. Rare earth elements from magnesites and sediments CI carbonaceous chondrite-normalized. Magnesites from different depths are denoted with spherical symbols, and the sediments are denoted as the other symbols (Swindle, Vasconcelos, Dalleska, et al., 2025). The sizes and color intensity of the spheres decrease with depth (small light sphere means shallower magnesite, large black sphere is magnesite at 11.8 m). A depth trend suggests there is an increasing influence of the elements coming from the dissolving sands as the depth and amount of magnesite decrease. Magnesite is growing progressively from solutions coming from the bottom of the profile, and as Mg derived from the ultramafic source rocks increases, the REE signature from the dissolving sediments decreases.

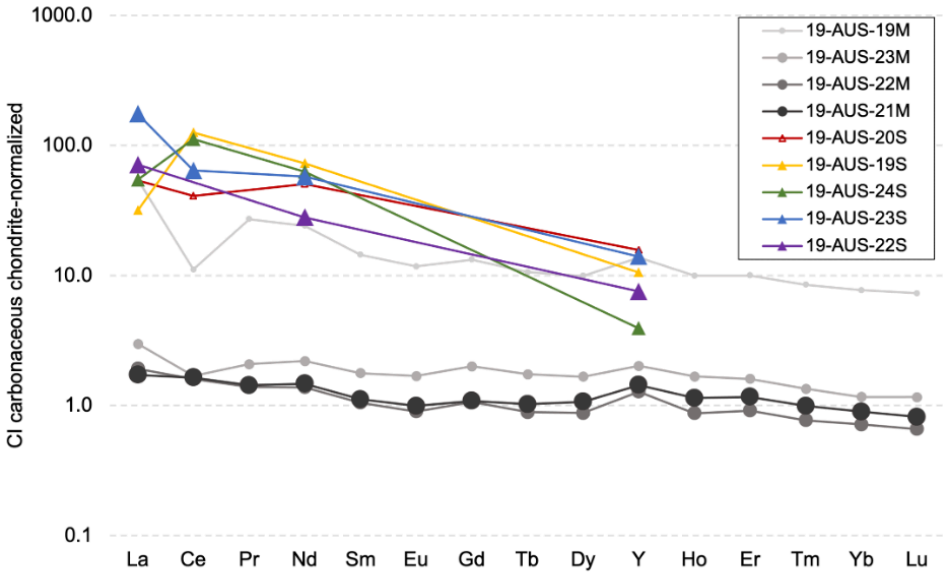

Figure 8. Conceptual diagram for the formation of magnesite and the sediments found in the sampled vertisol. Stages I-IV indicate formation and development through time.

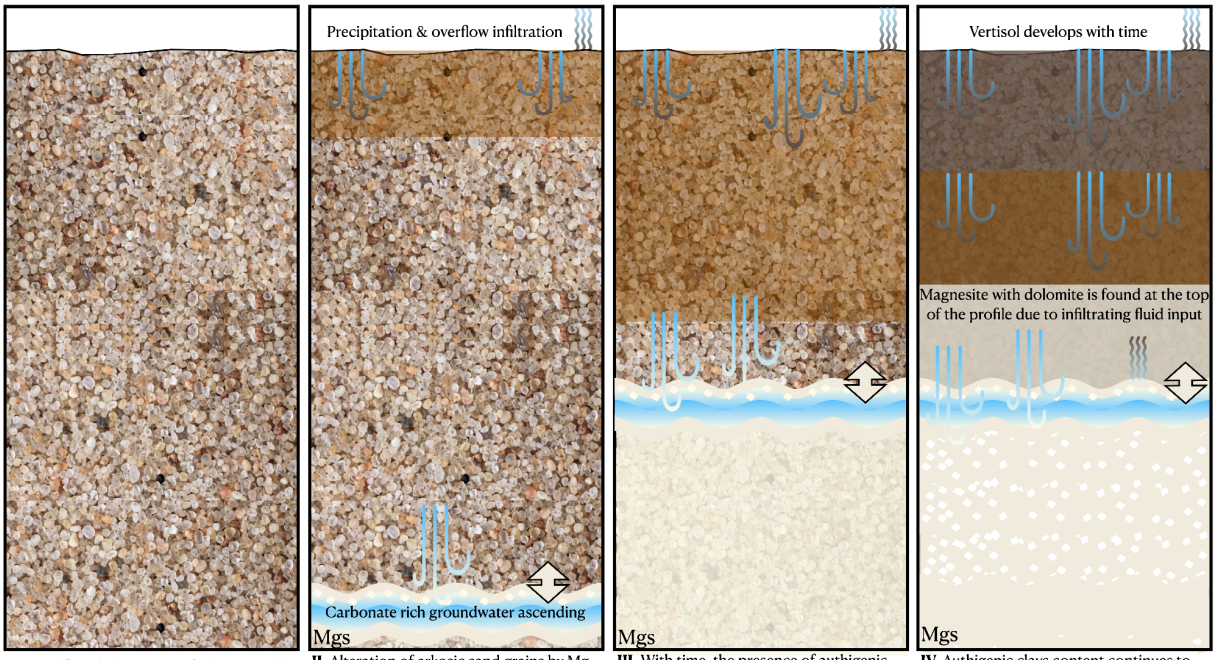

I. Initial fluvial deposition of arkosic sand weathered from nearby granodiorite/ granite outcrops

II. Alteration of arkosic sand grains by Mg-carbonation via fluctuating groundwater movement and evaporation which replaces quartz with magnesite and develops magnesite nodules at the groundwater interface. Soils develop due to resulting weathering products and magnesite forming.

III. With time, the presence of authigenic clays increases and magnesite increases within the profile as well as in purity developing magnecretes with nodules, while arkosic sand decreases.

IV. Authigenic clays content continues to increase with time and a vertisol develops. Magnesite continues to increase in the profile due to a fluctuating groundwater table as well as in purity at the profile base. Magnesite with dolomite is found at the top of the profile due to infiltrating fluids input.

Supplemental Figures

Table S1. Vertisol inventory of matrix samples and magnesite samples evaluated

Sample	**Depth (m, bgs)**	**Matrix**	**Magnesite**	**Identified mineralogical phases via microscopy & x-ray fluorescence**
19-AUS-20	0-6.8	Dark surficial clay with manganese nodules	-	-
19-AUS-19	6.8-8.3	Greenish-gray and brown clay with sand sized white carbonate grains	Friable gray magnesite/dolomite with clay-filled millimeter-scale pores	Magnesite, dolomite, limonite, rare chert, detrital quartz

19-AUS-24	8.3-9.3	Light gray clay with manganese oxide precipitates along fractures	Magnesite/dolomite with reddish-tan 3-5 millimeter-wide inclusions	Magnesite, dolomite, chert, detrital quartz, detrital plagioclase
19-AUS-23	9.3-10.3	Light gray clay with manganese oxide precipitates along fractures	Cryptocrystalline magnesite nodule with beige, cracked surface and circumgranular pores	Magnesite, minor chert, rare detrital quartz, rare detrital feldspar
19-AUS-22	10.3-11.3	Weakly indurated clayey, silty, very fine sand	Cauliflower-shaped cryptocrystalline magnesite nodule with millimeter-thick tan dendritic rind	Magnesite
19-AUS-21	11.3-12.3	-	Cryptocrystalline magnesite nodule with tan, cracked surface and millimeter-scale irregular pores	Magnesite, rare detrital quartz, rare detrital feldspar

Table S2. Sediment matrix quantitative XRD analysis. XRD-based matrix composition represented in percentage. Values are in weight percent of the specified minerals and phases total 100%. *R0 M-L I/S (90%S) - R0 (Random) Ordered Mixed-Layer Illite/Smectite with 90% Smectite Layers. Overall, swelling clays dominate, followed by quartz, which is both detrital and authigenic. The lower samples have immature detrital materials (e.g., plagioclase, K-feldspar, lizardite) and the upper samples do not. Dolomite and magnesite are only found in the matrix of the upper samples, though they are the predominant components of the nodules observed. Authigenic, aluminum-poor clay (palygorskite) increases in abundance from the bottom of the profile to 19-AUS-24, though it is absent in 19-AUS-19 and talc is found in the uppermost samples.

Sample ID	Quartz	K-Feldspar	Plagioclase	Dolomite	Hematite	Talc	Magnesite	Lizardite	Palygorskite	Illite&Mica	Kaolinite	R0 M-L I/S (90%S)*	TOTAL
19-AUS-20	23	0	0	0	0.2	1.3	0.5	0	0	1.4	0.4	73.2	100
19-AUS-19	23.4	0	0	2.4	0.2	1.9	1.2	0	0	1.3	0.5	69.1	100
19-AUS-24	8.6	0.9	2.3	0	0	0.5	0.2	0.2	3.1	0.8	0.5	82.9	100
19-AUS-23	9.5	1.2	6	0	0	0.5	0.2	0.6	1	1.2	0.3	79.5	100
19-AUS-22	32.5	1.5	2.5	0	0	0.5	0	0.4	0.4	0.6	0.2	61.4	100

Figure S1. XRD traces of the sediment matrix. Sediment X-ray diffraction patterns (Cu Kα radiation) are arranged by position in the vertical profile beginning with 19-AUS-20 at the top. For all profiles, counts (y-axis) are plotted by 2 θ (x-axis) and the diffraction patterns are colored by sediment matrix (blue) or magnesite (red). These profiles show examples of clay peak

identification (smectite, palygorskite, disordered dioctohedredral smectite (i.e. montmorillonite), and increased disorder in the middle of the profile. The magnesite patterns show magnesite as well as dolomite peaks in the upper section (19-AUS-19, 19-AUS-24), while the deeper depths indicate just magnesite peaks (19-AUS-23, 19-AUS-22, 19-AUS-21). Smectite and palygorskite traces are present in the middle depths in the sediment matrix. Clays, quartz, and dolomite are absent at the base of the profile.

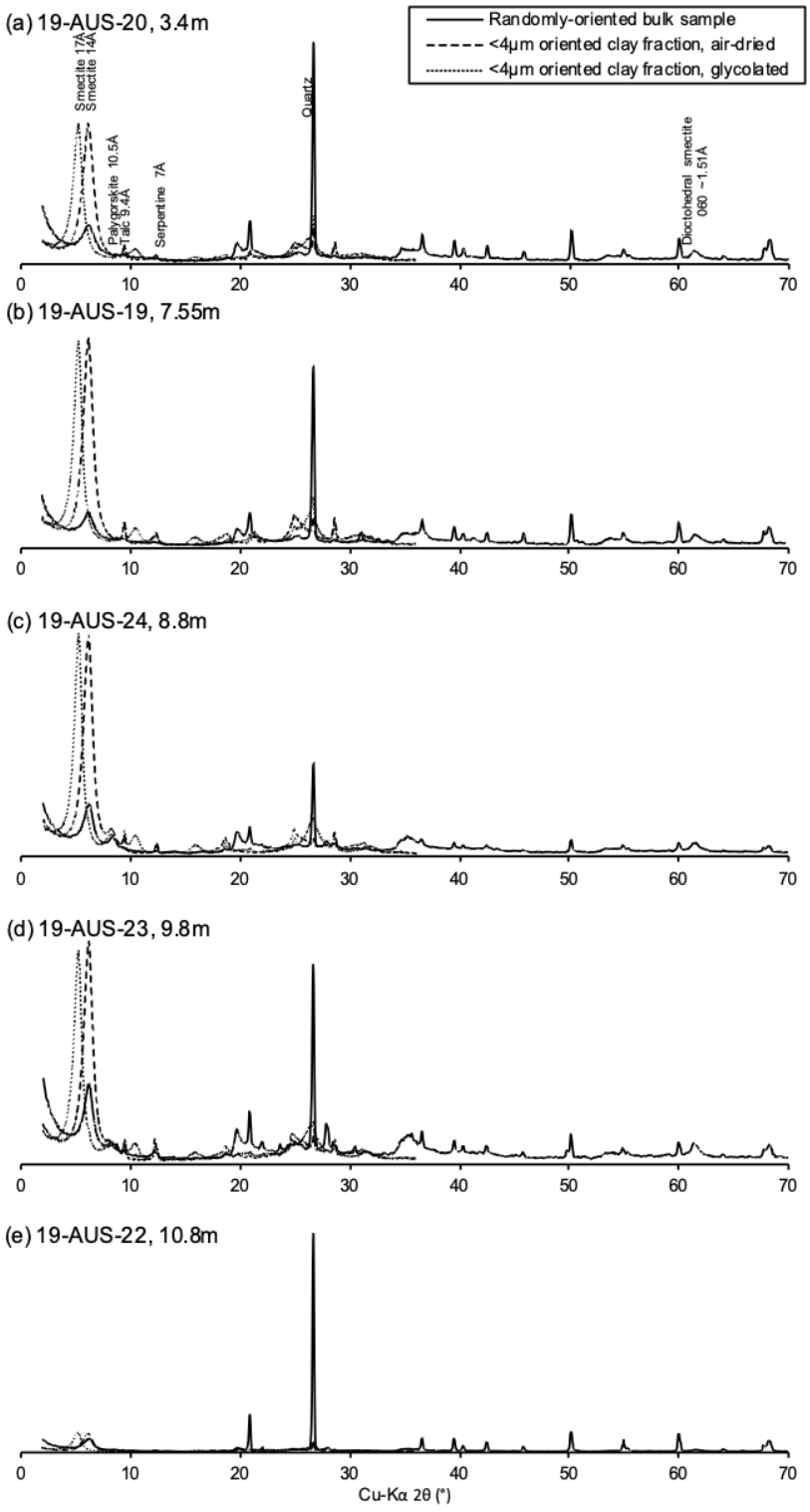

Figure S2. XRD traces of the matrix sediments and magnesites. X-ray diffraction patterns (Cu Kα radiation) are arranged by position in the vertical profile beginning with 19-AUS-20 at the top. For all profiles, counts (y-axis) are plotted by 2 θ (x-axis) and the diffraction patterns are colored by sediment matrix (blue) or magnesite (red). The magnesite patterns (Swindle et al., 2025) show magnesite as well as dolomite peaks in the upper section (19-AUS-19, 19-AUS-24, while the deeper depths indicate just magnesite peaks (19-AUS-23, 19-AUS-22, 19-AUS-21). Quartz is found in the matrix sediments in the top to middle depths of the profile. However, quartz and dolomite are absent at the base of the profile.

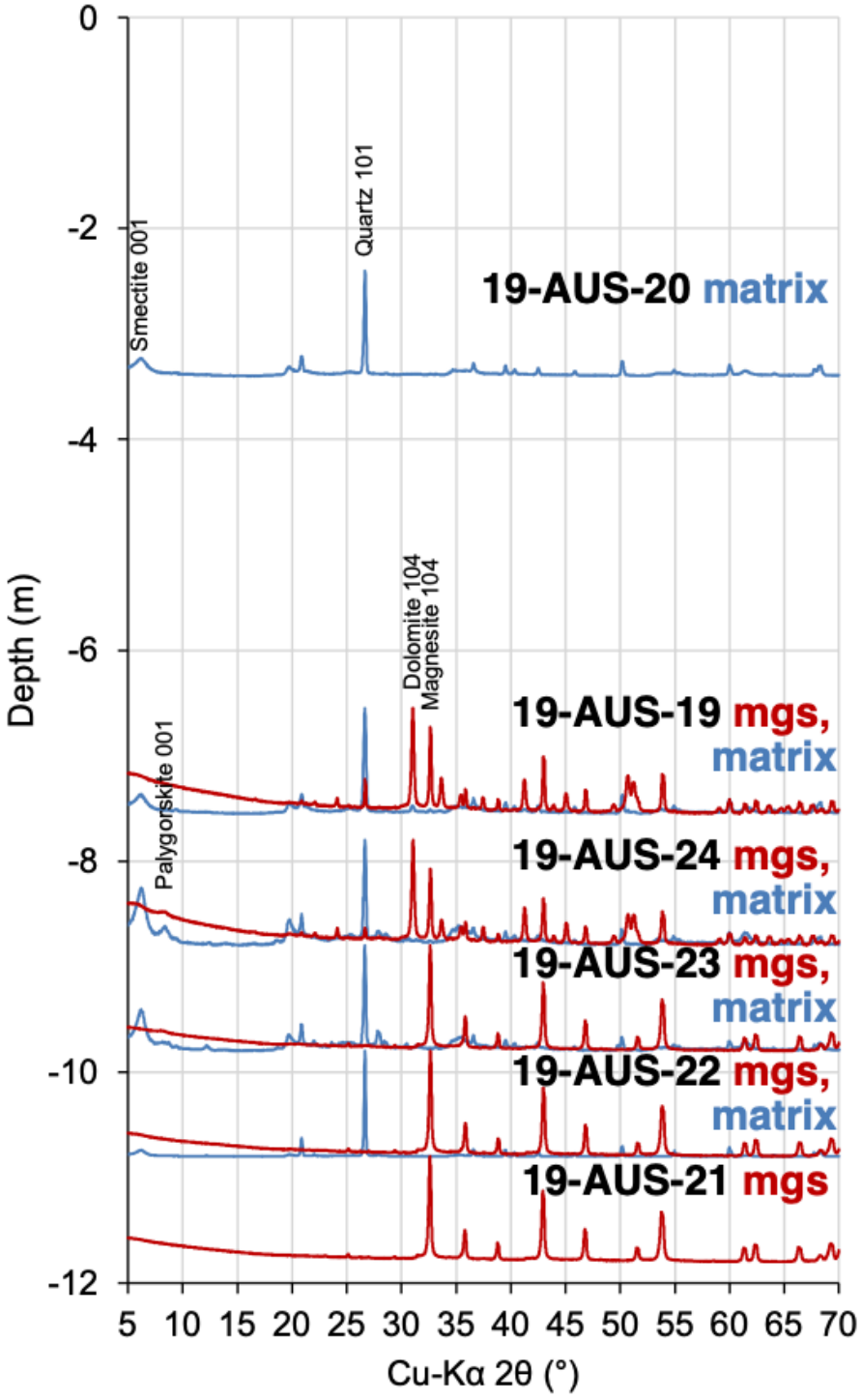

Figure S3. SEM sediment matrix clay textures. **(A, D)** Wavy subhedral clay (smectite) overgrowing an etched quartz grain, hyphae attached to ilmenite from sample 19-AUS-19. **(B, E)** MnOx rosettes overgrowing Fe-Al clays with cracks in sample 19-AUS-19 as well as carbonates (dolomite with some clay) bordering Fe-Al clays. In sample 19-AUS-24 **(C)**, we observed plagioclase grains being overgrown by flaky-textured Fe, Al, clays with micron sized carbonate phases. In sample 19-AUS-22 **(F)**, we observed rhombohedral light-toned grains interspersed within massive aggregates that appear clay-coated.